JOURNAL OF AIRCRAFT
Vol. 45, No. 3, May–June 2008

Numerical Simulation of Full-Span Delta Wing Buffet at High Angle of Attack

Peter J. Attar*
University of Oklahoma
and
Raymond E. Gordnier† and Miguel R. Visbal‡
U.S. Air Force Research Laboratory, Wright–Patterson Air Force Base, Ohio 45433-7913

DOI: 10.2514/1.28377

In this work, the buffet of a full-span, highly flexible, 50-deg-sweep delta wing at high angle of attack is studied using a computational aeroelastic solver. The aeroelastic solver couples a second-order finite difference solution of the Euler equations to a large-rotation nonlinear finite element structural solver. Particular attention is paid to the poststall region, in which previous experiments on highly flexible low-sweep delta wings have noted increased buffet response accompanied by lift enhancement and a delay in stall. It is thought that these phenomena are due to the reorganization of the flow and reformation of a leading-edge vortex structure. The nature of this enhanced lift is studied here for the flexible delta wing at an angle of attack of 25 deg and a flow velocity of 30 m/s. Using a prescribed wing motion, it is shown that it is possible to predict lift enhancement by solving only the inviscid Euler equations. The enhanced lift is due to a reorganization of the flow and the resulting region of increased suction near the apex of the wing. It is found that the mode of wing vibration has little influence on the enhanced lift phenomena, because both a prescribed symmetric first-mode motion and a prescribed antisymmetric third-mode motion led to lift enhancement. It is also insensitive to the wing vibration frequency for the range of frequencies tested, with the concession that below some minimum frequency, lift enhancement does not occur. The amplitude of wing vibration has some effect on the time-averaged lift coefficient. Fully coupled aeroelastic computations were also performed in this study for the wing. The fully aeroelastic computation did not predict the enhanced structural dynamic behavior and lift that was observed in the experiment. The dominant dynamic response of the wing was near the first mode, which has a frequency that is too low to initiate flow organization and the resulting enhanced lift due to increased suction.

Nomenclature

$\{a\}$	=	unit vector in the ξ direction
$\{b\}$	=	unit vector in the plane of the element and normal to $\{a\}$
$[C]$	=	damping matrix
c	=	root-chord length
c_{ijkl}	=	material constitutive tensor
$D(\,)$	=	material time-derivative operator
d_{kl}	=	time rate of the deformation tensor
E	=	material modulus of elasticity
e_{ij}	=	deformation tensor
$\{F\}$	=	vector of applied loads
$\hat{F}, \hat{G}, \hat{H}$	=	vectors of inviscid fluxes
f_i^B	=	component of body force
f_i^S	=	component of surface traction
h_i	=	thickness at node i
J	=	transformation Jacobian
$[K]$	=	tangent stiffness matrix
$[M]$	=	mass matrix
N_i	=	isoparametric shape functions
$\tilde{N}_i$	=	extra shape functions
q_s, q_d	=	prescribed-motion static and dynamic modal amplitudes
r	=	thickness coordinate
S	=	surface area of the deformed body over which tractions are applied
St	=	Strouhal number
s	=	semispan length
$\{U\}$	=	vector of nodal degrees of freedom
U_∞	=	freestream flow velocity
u_i	=	displacement in the i direction
u_x	=	displacement in the x direction
$u_{x,i}$	=	displacement in the x direction of node i
$\tilde{u}_{x,j}$	=	displacement in the x direction of the jth nodeless degree of freedom
u_y	=	displacement in the y direction
$u_{y,i}$	=	displacement in the y direction of node i
$\tilde{u}_{y,j}$	=	displacement in the y direction of the jth nodeless degree of freedom
u_z	=	displacement in the z direction
$u_{z,i}$	=	displacement in the z direction of node i
$\tilde{u}_{z,j}$	=	displacement in the z direction of the jth nodeless degree of freedom
V	=	volume of the deformed body
v_i	=	structural velocity
x_i	=	current coordinate
δ	=	represents spatial difference operator
$\theta_{x,i}$	=	rotation of node i about vector $\{a\}$
$\theta_{y,i}$	=	rotation of node i about vector $\{b\}$
ν	=	material Poisson ratio
ξ, η	=	element coordinate directions
ξ, η, ζ	=	computational coordinates
ρ_s	=	material density
σ_{ij}	=	Cauchy stress component

Presented as Paper 2075 at the 47th AIAA/ASME/ASCE/AHS/ASC Structures, Structural Dynamics, and Materials Conference, Newport, RI, 1–4 June 2006; received 16 October 2006; revision received 1 January 2008; accepted for publication 2 January 2008.

*Assistant Professor, Department of Mechanical and Aerospace Engineering; peter.attar@ou.edu. Member AIAA.
†Senior Research Aerospace Engineer, Computational Sciences Branch, Air Vehicles Directorate. Associate Fellow AIAA.
‡Technical Area Leader, Computational Sciences Branch, Air Vehicles Directorate. Associate Fellow AIAA

$\dot{\sigma}_{ij}$ = time rate of Cauchy stress
$\dot{\sigma}^{j}_{ij}$ = Jaumann rate of Cauchy stress
τ = nondimensional tU_∞/c
$\boldsymbol{\phi}_s, \boldsymbol{\phi}_d$ = prescribed-motion static and dynamic modal vectors
ϕ^i = constant used in determining fluid solver temporal accuracy
ω = nondimensional prescribed-motion frequency, St
$\dot{\omega}_{ik}$ = spin tensor

I. Introduction

UNMANNED air vehicle (UAV) and unmanned combat air vehicle (UCAV) configurations that are currently being developed contain highly flexible, low-sweep (40–60-deg) delta-wing-shaped planforms. These vehicles will need to be maneuverable, with the ability to fly at large angles of attack (greater than 20 deg). These two attributes, when combined with the high wing flexibility, will require detailed aeroelastic analysis to insure that the configurations do not suffer damage due to large static and/or dynamic deflections.

Extensive research has been conducted, both computational and experimental, on the unsteady vortical flows of rigid, highly swept (greater than 60 deg) delta wings. For a comprehensive review of this work, see the papers by Visbal [1] and Rockwell [2]. Significantly less research has been conducted to understand the unsteady flow characteristics of higher-aspect-ratio delta wings. Experimental [3,4] and computational results [5] have shown that the unsteady vortical flows for low-sweep delta wings are significantly different from those of higher-swept delta wings. This difference in the high-angle-of-attack behavior could also result in differences in the dynamic structural response of the wing.

Recently, research has been undertaken on the unsteady response of flexible moderate-to-low-sweep delta wings at high angle of attack. Experimental work by Gray et al. [6] was conducted on the buffeting of a moderately swept (60 deg) flexible delta wing. Computational work on the same configuration was conducted by Gordnier and Visbal [7]. In those computations, buffeting of the wing was not present at low angles of attack before vortex breakdown occurred. As the angle of attack increased, and vortex breakdown occurred and subsequently moved toward the apex of the wing, increased structural response was found. Once the breakdown reached the wing apex and the wing stalled, this response diminished. Both the experiment and computation exhibit this dynamic behavior of the wing.

Taylor et al. [8] conducted experiments on a highly flexible, 50-deg-sweep, full-span delta wing. In that work, large-amplitude structural vibrations in the second antisymmetric mode were observed in the poststall region. These structural vibrations were accompanied by a region of lift enhancement and significant delay in wing stall. Computations for a similar half-span 50-deg-sweep delta wing were conducted by Gordnier and Visbal [9], who used a nonlinear von Kármán plate theory for the structural model and a second-order finite difference solution of the Euler equations for the fluid model. This model achieved large dynamic oscillations, but did not capture the increased dynamic behavior and lift enhancement in the poststall region. Dynamic behavior in the poststall region, similar to that of the computed results of Gordnier and Visbal [9], was noted in a subsequent experimental investigation on a half-span model by Taylor et al. [8]. In experiments conducted by Vardaki et al. [10] on rolling oscillations of a rigid 50-deg-sweep delta wing, it was observed that the reformation of a leading-edge-vortex structure is influenced by the rolling frequency.

In the current work, we will investigate the increased dynamic behavior, lift enhancement, and delay in wing stall observed in [8] for the highly flexible, full-span, 50-deg delta wing. First, the importance of various parameters on the vortex reformation and lift-enhancement phenomena will be explored using prescribed wing motion. This will allow independent control of such parameters as frequency, dynamic and static wing deflections, and mode of vibration. Next, a computational aeroelastic solver will be used to explore the fully coupled aeroelastic problem. This solver is constructed by coupling a second-order finite difference solution of the Euler equations with a fully geometric nonlinear structural solver. A similar numerical method was previously used by the authors to compute the large-amplitude limit-cycle oscillations of a cropped delta wing in high subsonic/transonic flow [11]. In this work, the dynamic flow characteristics at a given dynamic pressure are greatly influenced by the accuracy of the computed structural deflections.

With the use of both the prescribed-motion and fully coupled solutions, the authors hope to gain a better understanding of the underlying physics of the problem and what needs to be included in the modeling to achieve an accurate solution. With this gained insight, it might then be possible to use this knowledge in the design of wings that use aeroelastic effects in a beneficial manner.

II. Theory

A. Aerodynamic Equations of Motion

The aerodynamic governing equations are the unsteady, compressible, three-dimensional Euler equations written in nondimensional strong-conservation-law form [12] employing a general time-dependent transformation. The resulting system of governing equations is expressed as

$$\frac{\partial \hat{U}}{\partial t} + \frac{\partial \hat{F}}{\partial \xi} + \frac{\partial \hat{G}}{\partial \eta} + \frac{\partial \hat{H}}{\partial \zeta} = 0.0 \tag{1}$$

With this formulation, the vector of dependent variables $\hat{U}$ is given as

$$\hat{U} = \frac{1}{J}U = \frac{1}{J}[\,\rho \quad \rho u \quad \rho v \quad \rho w \quad \rho E\,]^T \tag{2}$$

All variables were normalized by the appropriate combination of freestream density, velocity, and a characteristic length. The perfect-gas relationship closes the system of equations. Previous work with this delta wing [13] showed that an Euler calculation is sufficient to capture the primary vortical flow features resulting from flow separation from the sharp leading edge.

B. Discretization of the Aerodynamic Equations of Motion

Solutions of Eq. (1) are obtained numerically using the implicit, approximately factored, finite difference algorithm of Beam and Warming [14], employing a Newton-like subiteration procedure [15]. Second-order temporal accuracy is secured in this iterative approach by selecting $\phi = 1/2$ in Eq. (3). The numerical algorithm is written in approximately factored delta form as

$$\begin{aligned}
&\left[J^{-1^{p+1}} + \phi^i \Delta\tau_s \delta_\xi\left(\frac{\partial \hat{F}^p}{\partial U}\right)\right] J^{p+1} \\
&\quad \times \left[J^{-1^{p+1}} + \phi^i \Delta\tau_s \delta_\eta\left(\frac{\partial \hat{G}^p}{\partial U}\right)\right] J^{p+1} \\
&\quad \times \left[J^{-1^{p+1}} + \phi^i \Delta\tau_s \delta_\xi\left(\frac{\partial \hat{H}^p}{\partial U}\right)\right] \Delta U \\
&\quad = -\phi^i \Delta\tau_s \left[J^{-1^{p+1}} \frac{(1+\phi)U^p - (1+2\phi)U^n + \phi U^{n-1}}{\Delta\tau}\right. \\
&\quad - U^p \left(\left(\frac{\xi_\tau}{J}\right)_\xi + \left(\frac{\eta_\tau}{J}\right)_\eta + \left(\frac{\zeta_\tau}{J}\right)_\zeta\right)^{p+1} \\
&\quad \left. + \delta_\xi(\hat{F}^p) + \delta_\eta(\hat{G}^p) + \delta_\zeta(\hat{H}^p)\right]
\end{aligned} \tag{3}$$

where

$$\phi^i = \frac{1}{1+\phi}, \qquad \Delta U = U^{p+1} - U^p \tag{4}$$

For $p = 1$, $U^p = U^n$, and as $p \to \infty$, $U^p \to U^{n+1}$. In the preceding expression, the geometric conservation law

$$\frac{\partial J^{-1}}{\partial \tau} + \left(\frac{\xi_\tau}{J}\right)_\xi + \left(\frac{\eta_\tau}{J}\right)_\eta + \left(\frac{\zeta_\tau}{J}\right)_\zeta = 0.0 \tag{5}$$

was used to evaluate the term $\partial J^{-1}/\partial \tau$. which insures satisfaction of the geometric conservation law for moving meshes.

With this subiterative approach, the right-hand side of Eq. (3) represents the numerical approximation to the governing equation, whereas the left-hand side vanishes as $p \to \infty$. The left-hand side may therefore be modified without loss of formal accuracy, provided a sufficient number of subiterates is employed. In particular, diagonalizing the left-hand side of Eq. (3), following the approach of [16], improves the efficiency of the algorithm. Although the diagonalized form of the alternating-direction-implicit scheme is only first-order time-accurate, when coupled with subiterations, higher-order time accuracy may be recovered [17]. Furthermore, a time step $\Delta\tau_s$ on the left-hand side of the equation may be chosen independently from the physical time step $\Delta\tau$ on the right-hand side, thereby enhancing stability. The right-hand side of Eq. (3) may also be modified to include a higher-order upwind-biased algorithm (Roe scheme [18]), lagged boundary conditions, or lagged turbulence modeling without destroying the implicit nature of the algorithm.

In Eq. (3), all spatial derivatives are approximated by second-order-accurate central differences, and common forms of both implicit and explicit nonlinear dissipation [19] are employed to preserve numerical stability. The temporal metric derivatives are discretized in a manner consistent with the temporal derivative of the conserved variables in Eq. (3).

When solving fluid/structure interaction problems, the aerodynamic mesh must be allowed to move in accordance with the motion of the structural surface. A simple algebraic method described in [20] deforms the aerodynamic mesh to accommodate the changing surface position. In this paper, the mesh is only moved in the z direction. This grid-motion strategy has proved adequate for the plate motions considered in the present work.

C. Structural Equations of Motion

The ANSYS commercial finite element code [21] is used as the nonlinear structural solver. The principle of virtual work in combination with a Rayleigh–Ritz solution in the form of finite element analysis is employed to develop a system of nonlinear differential equations. The general form of the equations in matrix notation is

$$[M]\{\ddot{U}\} + [C]\{\dot{U}\} + [K]\{U\} = \{F\} \tag{6}$$

where $\{U\}$ is the vector of nodal degrees of freedom; $[M]$, $[C]$, and $[K]$ are the mass, damping, and stiffness matrices, respectively; and $\{F\}$ is the vector of applied loads (which, in this analysis, are due to pressure on the wing). A Rayleigh damping model is used, with the damping expressed as a linear combination of the mass and stiffness matrices.

The element stiffness is formulated based on the principal of virtual work:

$$\int_V \sigma_{ij}\delta e_{ij}\,\mathrm{d}V = \int_V f_i^B \delta u_i\,\mathrm{d}V + \int_S f_i^S \delta u_i\,\mathrm{d}S \tag{7}$$

In this section, index notation is used in which repeated subscripts imply summation on the possible range of the subscript. In Eq. (7), σ_{ij} is a Cauchy stress component and e_{ij} is the deformation tensor defined as

$$e_{ij} = \frac{1}{2}\left(\frac{\partial u_i}{\partial x_j} + \frac{\partial u_j}{\partial x_i}\right) \tag{8}$$

Because Cauchy stress is affected by rigid-body motion and objective (frame-invariant) stresses are needed in the constitutive law used to relate stress and strain, Cauchy stress by itself cannot be used in the element formulations. In the current work, the Jaumann rate of Cauchy stress $\dot{\sigma}_{ij}^J$, as expressed by McMeeking and Rice [22], is used:

$$\dot{\sigma}_{ij}^J = \dot{\sigma}_{ij} - \sigma_{ik}\dot{\omega}_{jk} - \sigma_{jk}\dot{\omega}_{ik} \tag{9}$$

where $\dot{\omega}_{ik}$ is the spin tensor defined as

$$\dot{\omega}_{ik} = \frac{1}{2}\left(\frac{\partial v_i}{\partial x_j} - \frac{\partial v_j}{\partial x_i}\right) \tag{10}$$

$\dot{\sigma}_{ij}$ is the time rate of Cauchy stress, and v_i is the structural velocity.

The time rate of the material constitutive law can be written as

$$\dot{\sigma}_{ij}^J = c_{ijkl} d_{kl} \tag{11}$$

where c_{ijkl} is the material constitutive tensor, and d_{kl} is the time rate of deformation tensor defined as

$$d_{ij} = D(e_{ij}) = \frac{1}{2}\left(\frac{\partial v_i}{\partial x_j} + \frac{\partial v_j}{\partial x_i}\right) \tag{12}$$

where $D(\,)$ is the material time-derivative operator. Using Eqs. (9) and (11), the Cauchy stress rate can then be written as

$$\begin{aligned}\dot{\sigma}_{ij} &= c_{ijkl} d_{kl} + \sigma_{ik} D(\omega_{jk}) + \sigma_{jk} D(\omega_{ik}) = c_{ijkl} D(e_{kl}) \\ &\quad + \sigma_{ik} D(\omega_{jk}) + \sigma_{jk} D(\omega_{ik})\end{aligned} \tag{13}$$

The element stiffness formulation can then be obtained by differentiating the internal component of the virtual work:

$$\begin{aligned}D\int_V \sigma_{ij}\delta e_{ij}\,\mathrm{d}V &= \int_V D(\sigma_{ij})\delta e_{ij}\,\mathrm{d}V + \int_V \sigma_{ij} D(\delta e_{ij})\,\mathrm{d}V \\ &\quad + \int_V \sigma_{ij}\delta e_{ij} D(\,\mathrm{d}V)\end{aligned} \tag{14}$$

where the time derivative of $\mathrm{d}V$ can be written as

$$D(\mathrm{d}V) = \frac{\partial D u_k}{\partial x_k}\,\mathrm{d}V = D(e_{ii})\,\mathrm{d}V \tag{15}$$

Using Eqs. (13) and (15), Eq. (14) can be rewritten as

$$\begin{aligned}D\int_V \sigma_{ij}\delta e_{ij}\,\mathrm{d}V &= \int_V \delta e_{ij} c_{ijkl} D(e_{kl})\,\mathrm{d}V + \int_V \sigma_{ij}\left(\frac{\partial \delta u_k}{\partial x_i}\frac{\partial D(u_k)}{\partial x_j}\right. \\ &\quad \left. - 2\delta e_{ik} D(e_{kj})\right)\mathrm{d}V + \int_V \delta e_{ij}\sigma_{ij}\frac{\partial D(u_k)}{\partial x_k}\,\mathrm{d}V\end{aligned} \tag{16}$$

In Eq. (16), the last integral is asymmetric and usually insignificant, and so it is not included in the formulation. Therefore, the final form is written as

$$\begin{aligned}D\int_V \sigma_{ij}\delta e_{ij}\,\mathrm{d}V &= \int_V \delta e_{ij} c_{ijkl} D(e_{kl})\,\mathrm{d}V \\ &\quad + \int_V \sigma_{ij}\left(\frac{\partial \delta u_k}{\partial x_i}\frac{\partial D(u_k)}{\partial x_j} - 2\delta e_{ik} D(e_{kj})\right)\mathrm{d}V\end{aligned} \tag{17}$$

This equation is a linear function of the change in displacement $D(u_i)$ and is identical to the form published by McMeeking and Rice [22]. The first integral in Eq. (17) is the material stiffness and the second term is due to geometric nonlinearity. An updated Lagrangian approach is used to simulate geometric nonlinearity.

To derive the matrix equations, Eqs. (6) and (17) and the corresponding integrals due to body and external forcing [Eq. (7)] are approximated using the standard finite element procedure. The integrals in Eq. (17) are discretized by writing the x, y, and z displacements (u_x, u_y, and u_z, respectively) in terms of the nodal displacements in the following manner:

$$\begin{Bmatrix} u_x \\ u_y \\ u_z \end{Bmatrix} = \sum_{i=1}^{4} N_i \begin{Bmatrix} u_{x,i} \\ u_{y,i} \\ u_{z,i} \end{Bmatrix} + \sum_{j=1}^{2} \tilde{N}_j \begin{Bmatrix} \tilde{u}_{x,j} \\ \tilde{u}_{y,j} \\ \tilde{u}_{z,j} \end{Bmatrix} + \sum_{i=1}^{4} N_i \frac{rh_i}{2} \begin{bmatrix} a_{1,i} & b_{1,i} \\ a_{2,i} & b_{2,i} \\ a_{3,i} & b_{3,i} \end{bmatrix} \begin{Bmatrix} \theta_{x,i} \\ \theta_{y,i} \end{Bmatrix} \tag{18}$$

where the isoparametric shape functions N_i are defined as

$$N_1 = \tfrac{1}{4}(1-\xi)(1-\eta) \qquad N_2 = \tfrac{1}{4}(1+\xi)(1-\eta)$$
$$N_3 = \tfrac{1}{4}(1+\xi)(1+\eta) \qquad N_4 = \tfrac{1}{4}(1-\xi)(1+\eta) \tag{19}$$

and the extra shape functions $\tilde{N}_j$, used to prevent shear locking, are written as

$$\tilde{N}_1 = (1-\xi^2) \qquad \tilde{N}_2 = (1-\eta^2) \tag{20}$$

The body and applied loading integrals from Eq. (7) are discretized using the isoparametric shape functions of Eq. (19).

Because the integrals in Eq. (7) are a function of the unknown displacements, the final discretized system of equations represented in Eq. (6) is nonlinear in the displacements. To solve Eq. (6) for the unknown nodal displacements, a Newton–Raphson iteration is used. Finally, the average acceleration form of the implicit Newmark family of integration methods is used to advance the structural solution forward in time. The average-acceleration Newmark method has second-order temporal accuracy.

D. Fluid–Structure Coupling

To model aeroelastic phenomena, the structural and aerodynamic models must be coupled. In the structural equation (6), this coupling is due to the pressure load vector $\{F\}$. In the aerodynamic system, the coupling comes from the resulting wing deflection u_z.

To achieve implicit coupling of the aerodynamic and structural equations, the subiteration procedure described in Sec. II.B is replaced with a global subiteration. During each subiteration, the aerodynamic forces on the structure are updated and the aerodynamic mesh is moved using updated structural displacements. The use of a subiteration procedure to implicitly couple the two physics models reduces any temporal lag that may have existed due to the loose coupling of the models, with complete synchronization of the equation sets achieved. The importance of synchronizing the loosely coupled systems was demonstrated in [23]. The fluid solver factorization and linearization errors are also eliminated using the global subiteration strategy. The resulting coupled procedure retains second-order temporal accuracy.

The fluid solver and mesh-motion algorithm used in this work are parallelized. Therefore, to achieve an efficient coupled aeroelastic solution, it is advantageous to advance the fluid and structure simultaneously within each subiteration. Within this framework, information (loads and deflections) from the previous subiteration is exchanged before each new subiteration.

Different grid topologies are used for the computational fluid dynamics (CFD) grid and the structural grid on the surface of the wing. Therefore, interpolation of the loads and displacements between the structural and aerodynamic grids is necessary. The interpolation of the fluid loads from the CFD grid points to the structural nodes is accomplished using a load-conserving algorithm [24]. This method uses finite element shape functions to interpolate from the CFD mesh to the structural mesh. Bilinear shape functions are used in the interpolation. The deflections are interpolated from the structural nodes to the fluid mesh points using a thin-plate spline interpolation.

E. Boundary Conditions

The aerodynamic boundary conditions for the delta wing are as follows. On the wing, conditions enforcing flow tangency to the moving surface are applied. The pressure is obtained from the expression $\partial p/\partial n = -\rho \boldsymbol{a}_b \cdot \boldsymbol{n}$, where $\boldsymbol{a}_b$ is the acceleration of the body and $\boldsymbol{n}$ is a vector normal to the surface. The density on the surface is determined by extrapolation from the interior points. At the outflow boundary downstream, all variables are extrapolated from the interior using a first-order extrapolation. Quasi-1-D characteristic boundary conditions are applied at all other far-field boundaries.

III. Delta-Wing Model

The delta-wing geometry investigated experimentally by Taylor et al. [8] (Fig. 1) consists of a flat-plate aluminum delta wing with a leading-edge sweep angle $\Lambda = 50\,\text{deg}$, a root-chord length $c = 0.310$ m, and a thickness of 0.001 m. For the finite element modeling, the structural properties of the aluminum wing are taken to be $\rho_s = 2700\ \text{kg/m}^3$, $E = 6.9 \times 10^{10}\ \text{N/m}^2$, and $\nu = 0.33$, where ρ_s is the density, E is the modulus of elasticity, and ν is the Poisson ratio. The structural finite element mesh, shown in Fig. 2, is constructed using 1144 four-node shell elements (see Sec. II.C for more details on this element). The finite element model contains a total of 7494 degrees of freedom. A fully clamped boundary condition is applied along the edge of the portion of the model that is in contact with the support. The support itself is not modeled.

The first three structural modes of the delta wing are shown in Figs. 3a–3c. The first two modes are symmetric and antisymmetric first bending modes, and the third mode is an antisymmetric combined bending-torsion mode. The computed frequencies of these modes are as follows: mode 1 is 23.03 Hz, mode 2 is 23.04 Hz, and mode 3 is 78.52 Hz. These correspond to Strouhal numbers of 0.238, 0.238, and 0.811, respectively.

The CFD grid employed for this delta-wing geometry consists of 141 points in the axial direction, 261 points in the spanwise direction, and 119 points in the body-normal direction. A total of 80 uniformly distributed points ($\Delta x = 0.0125$) are located in the axial direction, and 161 points are located on the wing in the spanwise direction. At the trailing edge, these points are distributed with a minimum spacing at the leading edge of $\Delta y = 0.0014$ and are stretched to a uniform spacing of $\Delta y = 0.018182$ over a majority of the wing; 75 points are located above the wing, with a minimum spacing at the wall ($\Delta z = 0.001$), and 53 points are used to resolve the vortical flow region at the trailing edge. The nondimensional time step used to advance both the fluid and structural solvers forward in time is $\Delta\tau = 0.0005$.

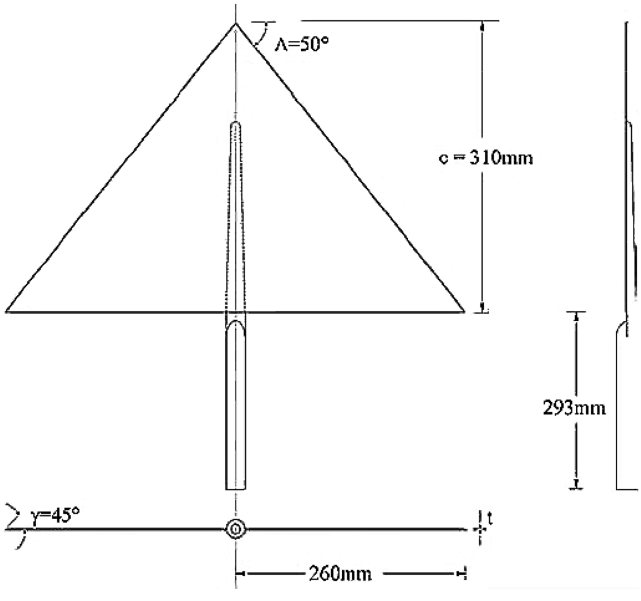

Fig. 1 Geometry of the delta wing.

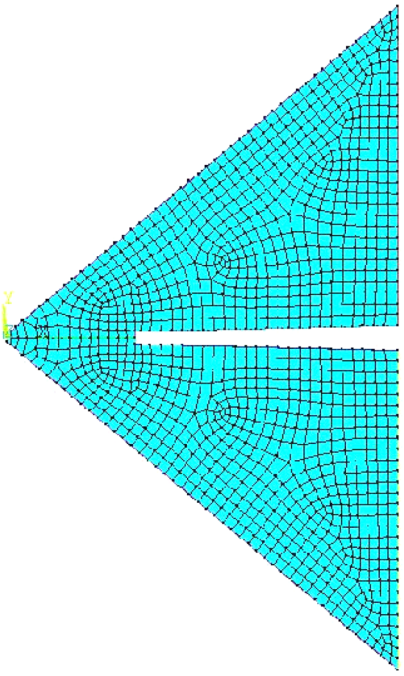

Fig. 2 Computational grid for the finite element structural model.

IV. Results

Experimental measurements for both rigid (0.005-m-thick) and flexible (0.001-m-thick) 50-deg-sweep delta wings were conducted by Taylor et al. [8,25] in the 2.13×1.52 m closed-circuit wind tunnel at the University of Bath. The maximum blockage of the tunnel was approximately 3.4% at $\alpha = 35$ deg. The experiments were conducted at a constant freestream velocity of 30 m/s.

Shown in Fig. 4 is a comparison of the measured [8] rms wing-tip acceleration at a flow speed of 30 m/s as a function of angle of attack for both half-span and full-span 50-deg delta wings. Note that at up to 22 deg, the rms response is similar for both models. However, starting at 23 deg, the full-span model shows a dramatic increase in the dynamic response, whereas the half-span model's dynamic response decreases. Accompanying this increase in dynamic response is a switch in the dominant mode of vibration from a predominantly first- or second-mode response to a predominantly third-mode response [8]. In the full-span model, this increase in dynamic response is accompanied by an increase in lift coefficient and a delay in wing stall. In Fig. 5, the lift coefficient for the full-span model is plotted vs angle of attack. Experimental and computational results are shown in the figure. The computational results will be discussed in the sections to follow. The region of lift enhancement is clearly visible starting at an angle of attack of 21 deg and extending all the way to an angle of attack of 29 deg. Hysteresis in the lift curve is also present, as shown by the dashed and dotted-dashed lines in Fig. 5. It should also be noted that the angle-of-attack region in which the increased dynamic behavior occurs and lift enhancement starts

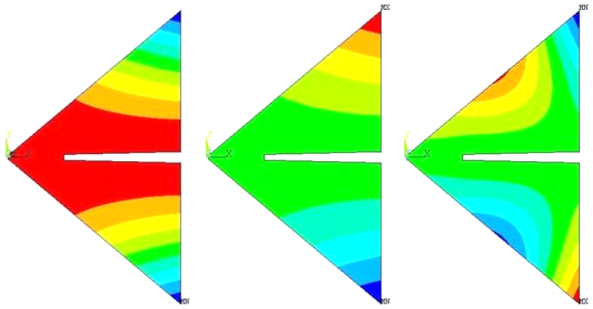

a) Mode 1 **b) Mode 2** **c) Mode 3**

Fig. 3 Structural modes of the delta wing.

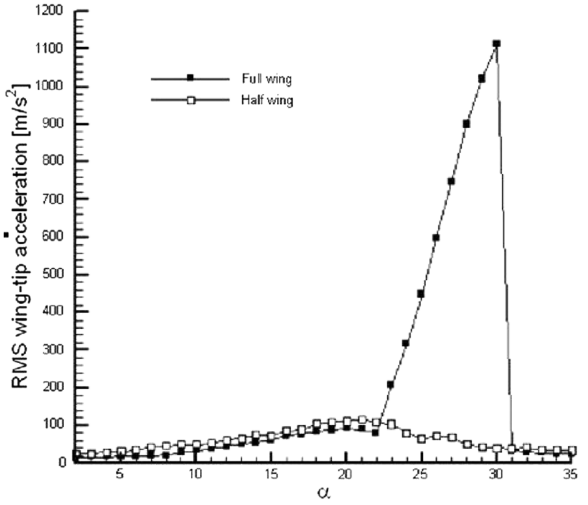

Fig. 4 Comparison of the experimentally measured [8] rms wing-tip acceleration for half-span and full-span 50-deg delta-wing models.

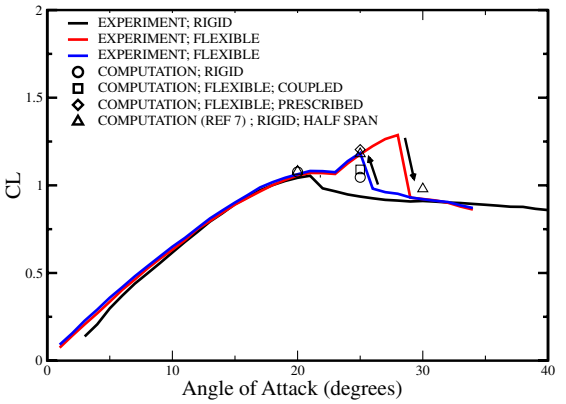

Fig. 5 Delta-wing time-averaged lift coefficient vs angle of attack.

corresponds to the region in which wing stall occurs for the rigid wing.

A. Rigid Wing

Shown in Figs. 6–8 are isosurface plots (at one instant in time) of normalized (by the freestream pressure) stagnation pressure for the full-span delta wing at 20 and 25 deg. The isosurfaces are shaded by axial velocity normalized by the freestream velocity. Figures 6 and 7

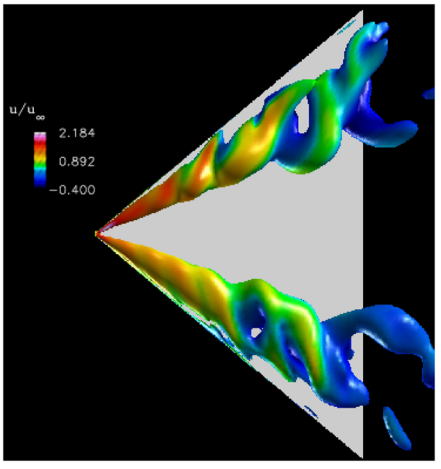

Fig. 6 Isosurface of normalized stagnation pressure shaded by normalized axial velocity at one instant in time for the full-span delta-wing computation at 20 deg.

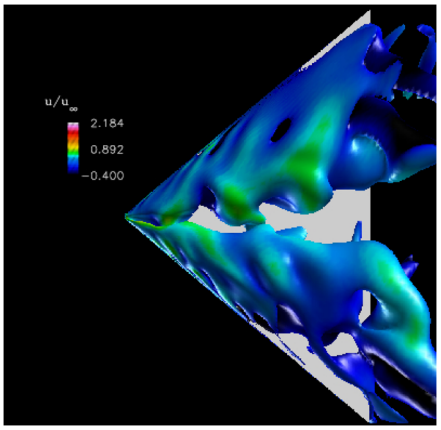

Fig. 7 Isosurface of normalized stagnation pressure shaded by normalized axial velocity at one instant in time for the full-span delta-wing computation at 25 deg.

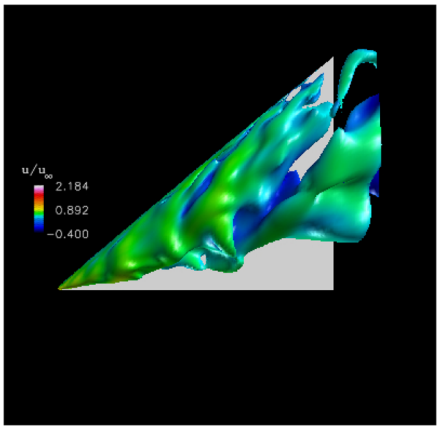

Fig. 8 Isosurface of normalized stagnation pressure shaded by normalized axial velocity at one instant in time for the half-span delta-wing computation at 25 deg.

show results for the full-span model, and the computation in Fig. 8 assumed symmetry in the flow solution at the wing centerline [9]. First note that the full-span solutions are not symmetric. Although this is not surprising, what is surprising is that whereas the full-span computations exhibit what looks to be stalled flow at 25 deg, the half-span model flow still appears fairly well organized, especially near the apex of the wing. Evidently, the constraint imposed by requiring the flow to be symmetric about the midspan delays the upstream propagation of vortex breakdown and the onset of stall. The result of this difference between the full-span and half-span solutions can be

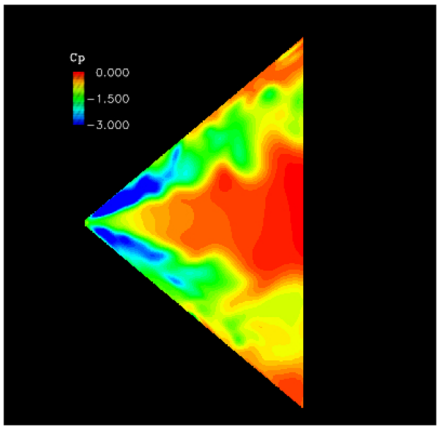

Fig. 9 Wing-surface C_p contours at one instant in time for the full-span delta-wing computation at 20 deg.

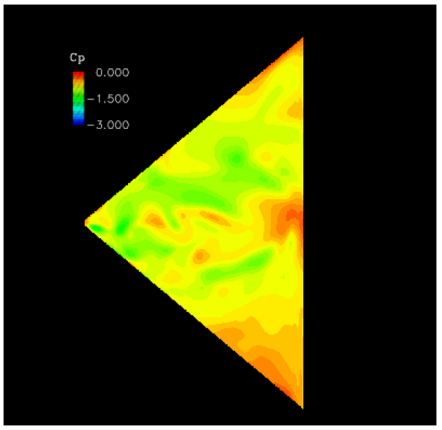

Fig. 10 Wing-surface C_p contours at one instant in time for the full-span delta-wing computation at 25 deg.

seen in the time-averaged lift-coefficient values shown in Fig. 5, in which the full-span rigid result does a better job of matching the rigid experiment data. Figures 9–11 show surface C_p contours for the full-span model computation at 20 and 25 deg and for the half-span model at 25 deg. Note that a region of low-pressure flow exists near the apex of the wing for both the full-span model at 20 deg and the half-span model at 25 deg, but is not present for the full-span model at 25 deg.

B. Prescribed Motion

To better understand the role of various parameters on the vortex reformation and lift-enhancement phenomena, computations were performed for a prescribed wing motion. The prescribed motion consisted of an out-of-plane z static deformation in the first mode and

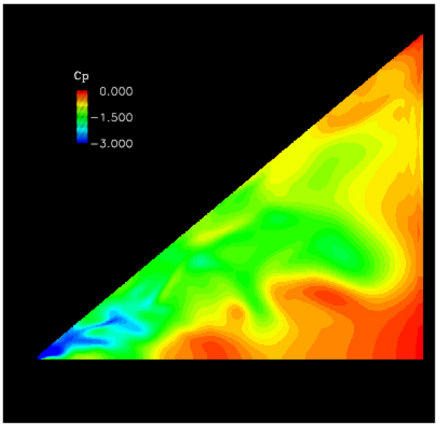

Fig. 11 Wing-surface C_p contours at one instant in time for the half-span delta-wing computation at 25 deg.

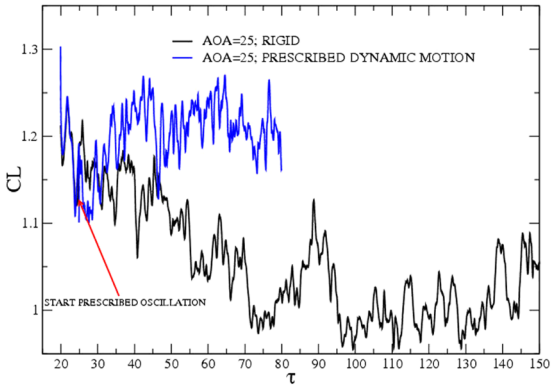

Fig. 12 Time history of the lift coefficient for the rigid wing and a prescribed motion with $\omega = 0.8$.

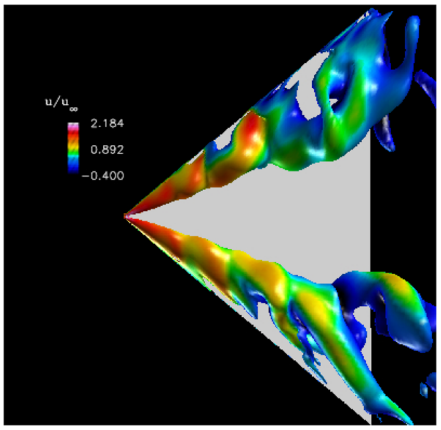

Fig. 13 Isosurface of normalized stagnation pressure shaded by normalized axial velocity at one instant in time for a prescribed motion in the third mode with $\omega = 0.8$.

then either a first-mode or third-mode dynamic portion. The time-dependent motion of the wing can be described in the following manner:

$$\boldsymbol{u}_z(x, y, \tau) = q_s \boldsymbol{\phi}_s(x, y) + q_d \boldsymbol{\phi}_d(x, y) \sin(\omega\tau) \tag{21}$$

where $q_s \boldsymbol{\phi}_s(x, y)$ is the static portion of the prescribed motion, $q_d \boldsymbol{\phi}_d(x, y) \sin(\omega\tau)$ is the dynamic portion of the prescribed motion, and $\omega = St$ is the nondimensional frequency. Here, the mode shape $\boldsymbol{\phi}_s(x, y)$ is the wing first mode and $\boldsymbol{\phi}_d(x, y)$ is either the wing first mode or third mode. The grid used in the computation of the modes has the same topology as the CFD surface grid. The computations are performed by ramping up the static deflection over five characteristic times while keeping the dynamic portion zero. Once the static deflection reached the maximum value, it is then held there for two characteristic times, after which the dynamic portion of the motion is initiated. All solutions are computed for $\alpha = 25$ deg and a flow velocity of 30 m/s.

The first question addressed is whether an inviscid computation is capable of predicting lift enhancement. Shown in Fig. 12 are lift-coefficient time histories for the rigid full-span delta wing and a prescribed-motion case. The values of the various parameters for this prescribed motion were as follows: $q_s = 0.17$, $q_d = 0.1$, and $\omega = 0.8$. The dynamic motion was in the third mode. From this figure, it is quite clear that the prescribed motion of the wing causes lift enhancement. The corresponding time-averaged lift-coefficient value is shown in Fig. 5 for $\alpha = 25$ deg and is denoted as "computation; flexible; prescribed." Shown in Fig. 13 is an isosurface of stagnation pressure at an instant in time for the prescribed motion in this case. Note that the flow appears more organized than the rigid-wing flow solution at this angle of attack in Fig. 7, and there exists a region of suction near the apex (Figs. 14a–14f). Once the flow becomes organized, it appears that the region of suction near the apex exists throughout the prescribed-motion cycle (Figs. 14a–14f and 15).

In water-tunnel experiments with a rigid wing undergoing small-amplitude rolling motion, Vardaki et al. [10] showed that flow that is totally separated for a stationary wing becomes increasingly organized as the frequency of rolling is increased. In the experiments, if the frequency was high enough, vortex reformation was noted and vortex breakdown was delayed when compared with the stationary wing. To investigate the effect of Strouhal number on the lift enhancement for a flexible wing, computations were performed using several different oscillation frequencies while keeping all other

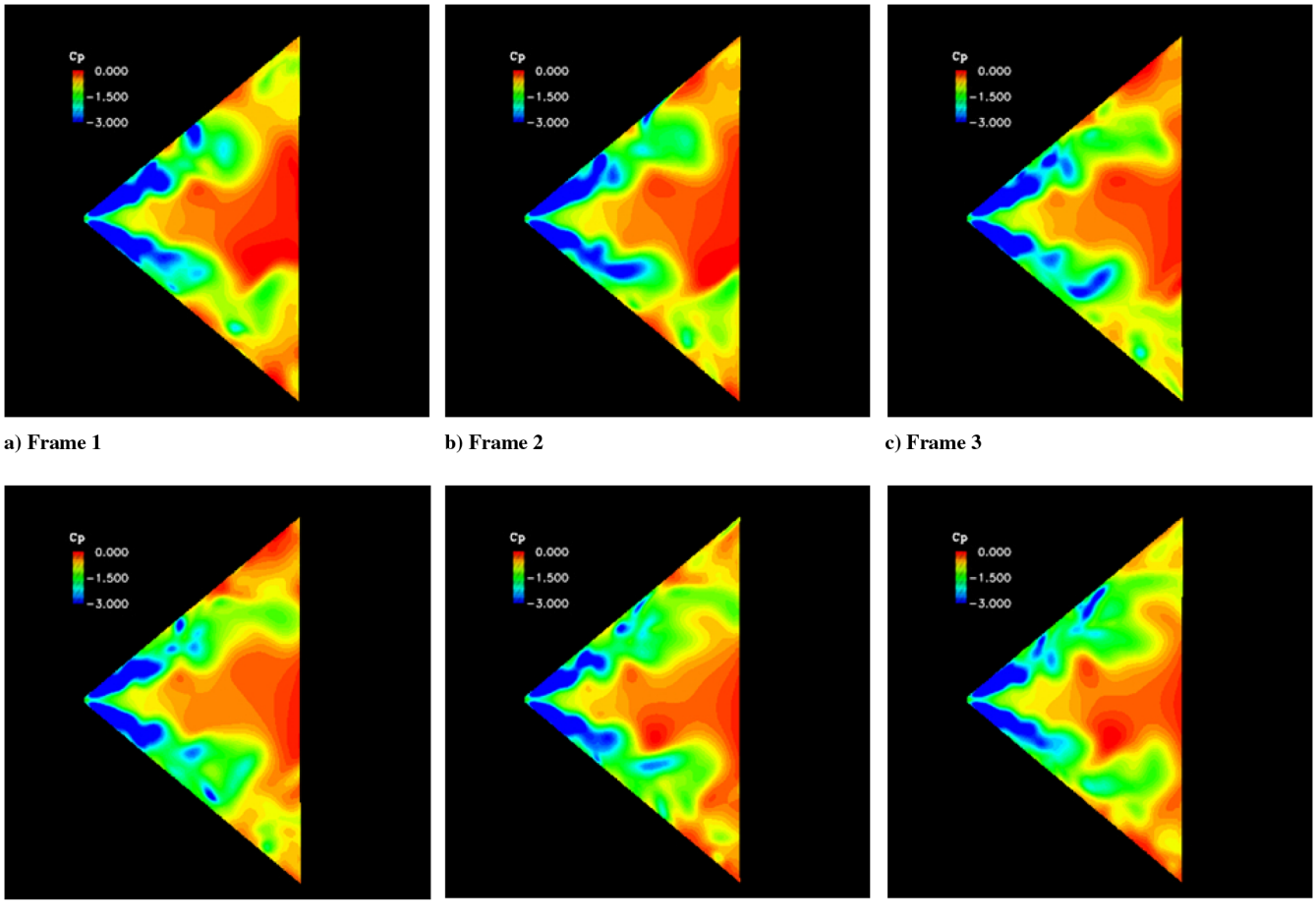

a) Frame 1 **b) Frame 2** **c) Frame 3**

d) Frame 4 **e) Frame 5** **f) Frame 6**

Fig. 14 Contours of wing surface C_p over one period of prescribed motion.

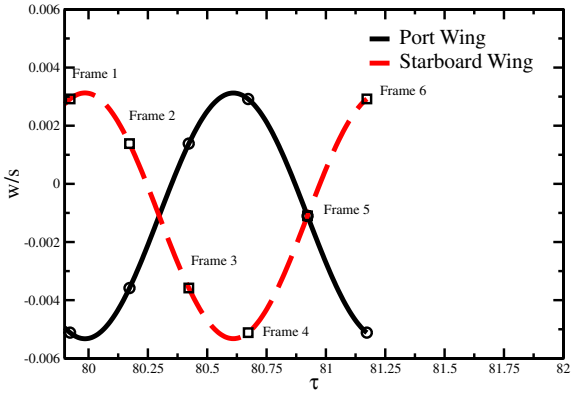

Fig. 15 Wing-tip deflection over one period of prescribed motion.

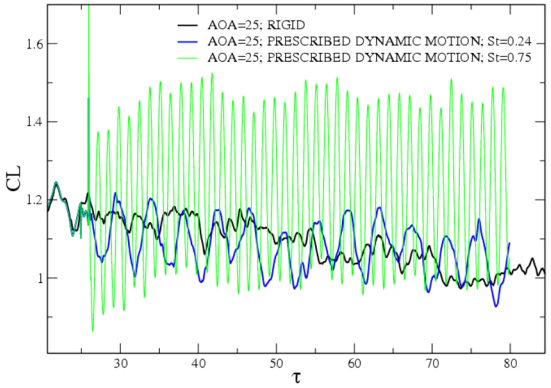

Fig. 16 Time history of the lift coefficient for the rigid wing and prescribed motions in the first mode with $\omega = 0.24$ and $\omega = 0.75$.

parameters constant. The time-averaged lift coefficients resulting from those calculations are shown in Table 1. In those computations, the dynamic motion of the wing is in the third mode $[\boldsymbol{\phi}_d(x, y) = \boldsymbol{\phi}_3(x, y)]$, with an amplitude of $q_d = 0.1$. This results in a maximum dynamic peak-to-peak amplitude of $w/s = 0.058$. The static modal amplitude is $q_s = 0.17$, which results in a maximum static tip deflection of $w/s = 0.125$. The time-averaged lift coefficient is seen to be insensitive to the frequency of oscillation for the range of frequencies tested. Similar to the work in [10], however, there appears to be a minimum frequency below which flow reorganization and lift enhancement will not occur.

Shown in Fig. 16 are lift-coefficient time histories for the rigid wing at an angle of attack of 25 deg. Also presented are prescribed motions of the wing in the first mode $[\boldsymbol{\phi}_d(x, y) = \boldsymbol{\phi}_1(x, y)]$, with $\omega = 0.24$ and 0.75. The lower-frequency case, $\omega = 0.24$, does not undergo lift enhancement. The higher frequency, $\omega = 0.75$, showed lift enhancement. Therefore, this indicates that the mode of vibration need not be antisymmetric for flow reorganization and the resulting lift enhancement to occur.

To explore the sensitivity of the lift-enhancement phenomena to dynamic amplitude, four different prescribed-motion cases are examined. In each case, the wing has a maximum static tip deflection of $w/s = 0.125$ and the prescribed motion is in the third mode with $\omega = 0.7$. The results are shown Table 2, in which w_d/s is the normalized peak-to-peak wing-tip amplitude of the prescribed motion. Shown in Figs. 17a–17d are the corresponding stagnation-pressure isosurface plots at an instant in time (same time value for each). As the dynamic amplitude of the prescribed-motion increases, the flow becomes more organized. This results in the mean lift coefficient increasing with amplitude, due to the creation of higher suction on the wing (Table 2).

C. Aeroelastic Results

To numerically investigate the experimentally observed flexible-wing large dynamic response (Fig. 4) and enhanced lift (Fig. 5), coupled aeroelastic computations were performed at an angle of attack of 25 deg. Initially, computations for a rigid delta wing at 25 deg were conducted. The wing was then released and allowed to respond to the unsteady aerodynamics.

Figure 18 shows the wing-tip dynamic response. The corresponding mean tip deflection, peak-to-peak tip deflection, and rms acceleration are shown in Table 3, along with the experimental results and nonlinear structural model results from [9]. Two values, one for each wing tip, are shown for the current work. All values from the current work in Fig. 3 were computed after the initial transient had died out. The computed mean deflection and rms acceleration from the current work are much smaller than the experimental values, whereas the peak-to-peak deflections are comparable. The computed mean and peak-to-peak deflections are similar to those of [9], whereas the computed rms acceleration from the current work are smaller. The difference in rms acceleration between this work and the work of [9] can probably be attributed to the different computed flow solutions at this angle of attack, as seen in Figs. 6 and 8.

In the experiment, the increase in dynamic response in Fig. 4 is accompanied by a change from a first-mode (symmetric) to a third-mode (antisymmetric) response. This does not appear to occur in the current computation, because a spectral analysis of the deflection (Fig. 19a) and acceleration (Fig. 19b) shows the dominant response peak to be near the first mode for the deflection, with equal parts first mode and third mode for the acceleration. This is significant when one considers the results from Fig. 16, in which the prescribed motion was in the first mode, with a first-mode frequency of 0.24. It was determined that for this low frequency, enhanced lift was not predicted. This also appears to be true here, because the computed mean lift coefficient in Fig. 5 underpredicts that of the experiment. In Figs. 20 and 21, it is evident that the flow has not significantly reorganized and a low-pressure region near the apex has not formed.

Table 1 Lift-coefficient dependence on the Strouhal number of the prescribed motion

St	CL
0.5	1.211
0.6	1.204
0.7	1.204
0.8	1.203
0.9	1.191

V. Conclusions

This paper investigated the phenomena of lift enhancement for nonslender (50-deg sweep) delta wings at high angle of attack. Experiments for a highly flexible 50-deg-sweep delta wing exhibited sizeable mean and peak-to-peak deflections in the poststall region, along with a switch of the vibration mode. This structural response resulted in a region of enhanced lift and a delay in stall.

The current investigation consisted of two parts. The first considered a prescribed wing motion at an angle of attack of 25 deg and a flow velocity of 30 m/s. This study gave insight into the sensitivity of the enhanced lift phenomena to the wing vibration characteristics (frequency, amplitude, and mode). Through this study, it was shown that an inviscid Euler flow solution can predict lift enhancement due to structural vibration. The enhanced lift is due to a reorganization of the flow and the resulting low-pressure region

Table 2 Lift-coefficient dependence on the dynamic amplitude of the prescribed motion

w_d/s	CL
0.01	1.135
0.02	1.181
0.06	1.204
0.23	1.234

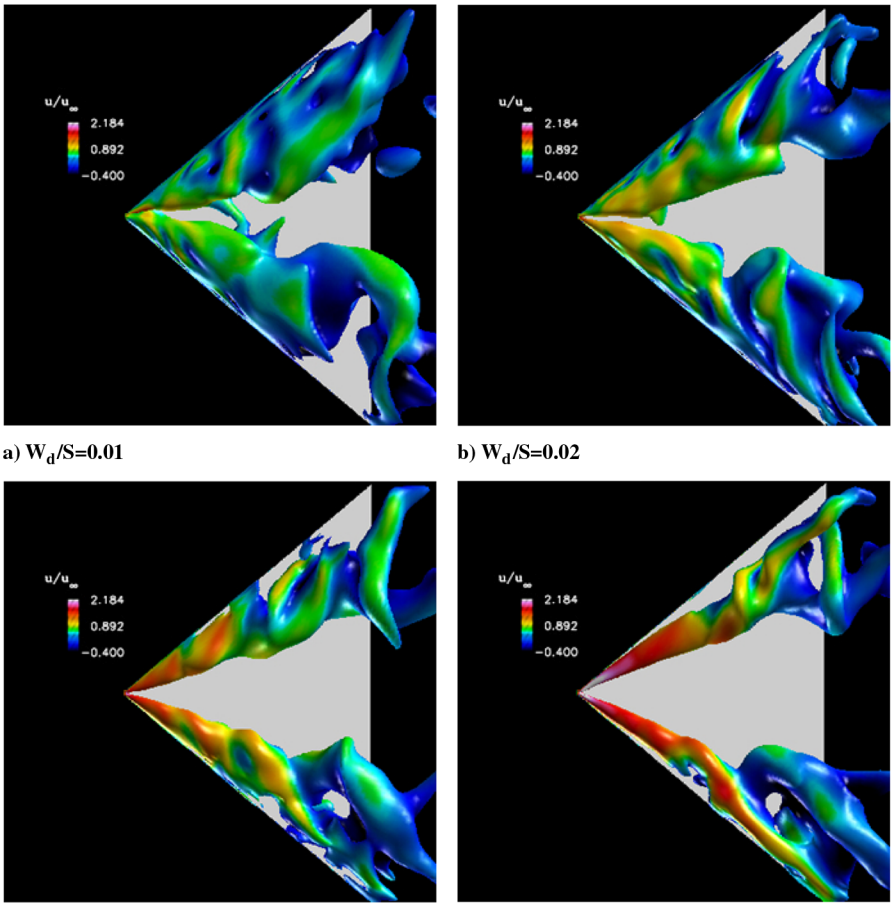

Fig. 17 Isosurface of normalized stagnation pressure shaded by normalized axial velocity at one instant in time for a prescribed motion in mode 3 with four different values of w_d/s.

that forms near the apex. The flow reorganization and enhanced lift were shown to have low sensitivity to vibration frequency, provided that the frequency was above some minimum value. These phenomena also appeared to be insensitive to the mode of vibration, because computations that had prescribed motion in the first mode (symmetric) and third mode (antisymmetric) both showed enhanced lift. Finally, the amplitude of vibration appeared to have a direct effect on the enhanced lift phenomena. As the amplitude was increased, the flow became more organized and the time-averaged lift increased.

The second portion of the investigation consisted of a coupled aeroelastic solution. An aeroelastic code that couples an Euler solver with a large-rotation geometrically nonlinear structural finite element solver was used for these computations. Strong coupling of the two solvers was accomplished using a subiteration approach that resulted in a solution that was second-order accurate in time. A computation was performed for the wing at an angle of attack of 25 deg and a flow velocity of 30 m/s. Unlike the experiment, a large rms acceleration was not predicted in the computations and lift enhancement was not evident. In the computation, the dominant deflection mode was near that of the first structural mode, which appeared to be too low of a frequency to excite the flow enough to organize it. This was true in the prescribed-motion investigation, in which it was shown that a wing vibration in the first mode with a first-mode frequency did not result in enhanced lift.

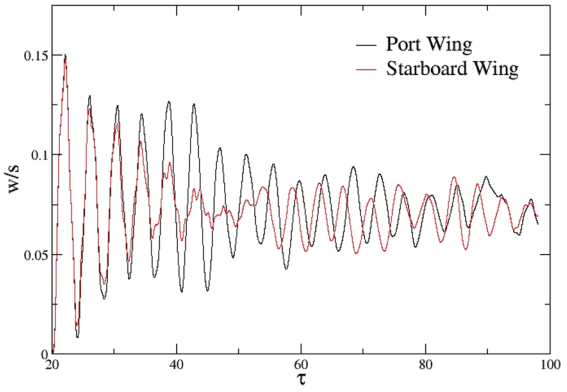

Fig. 18 Wing-tip dynamic response for the coupled aeroelastic problem.

The preceding results seem to indicate that for the coupled aeroelastic model to better match the experiment, the wing must be excited with a higher frequency. The wing excitation is due to unsteady pressure fluctuations on the surface, due to the stalled flow. Viscous effects play an important role in properly modeling wing stall. Inclusion of these effects may provide the appropriate fluid–structure interaction, resulting in the lift enhancement observed in experiment. Future computations will address this issue.

Table 3 Table of delta-wing structural response characteristics

	Mean w/s	Peak to peak w/s	rms acceleration (m/s^2)
Current	0.074, 0.072	0.043, 0.037	258.2, 247.6
Reference [9]	0.074	0.039	363.75
Experiment	0.122	0.055	448.33

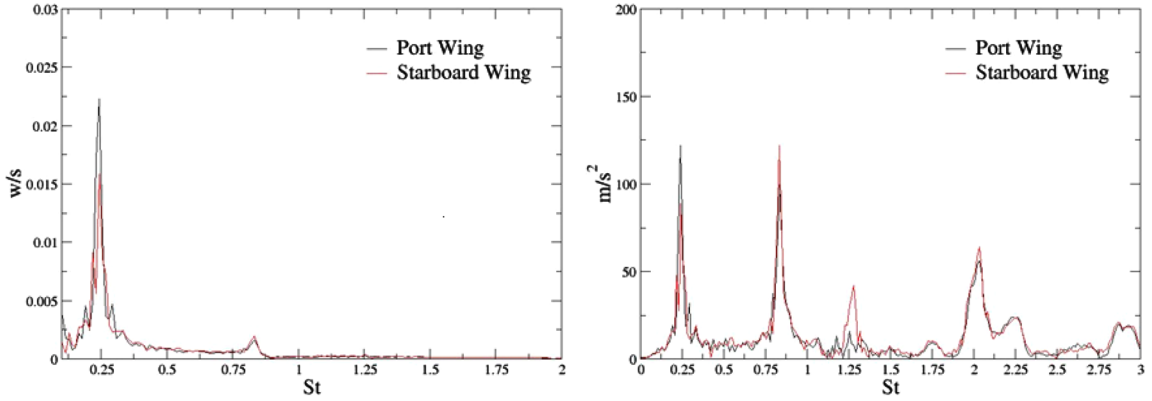

a) Deflection b) Acceleration

Fig. 19 Discrete Fourier transform of the wing-tip deflection and acceleration.

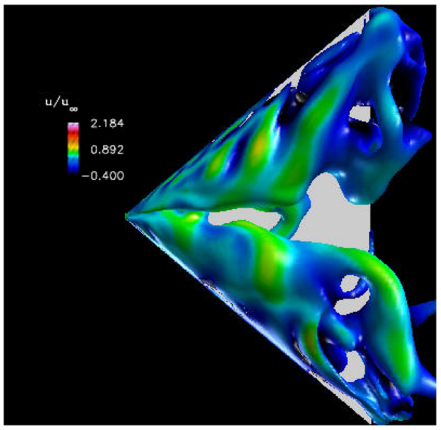

Fig. 20 Isosurface of normalized stagnation pressure shaded by normalized axial velocity at one instant in time for the coupled aeroelastic problem.

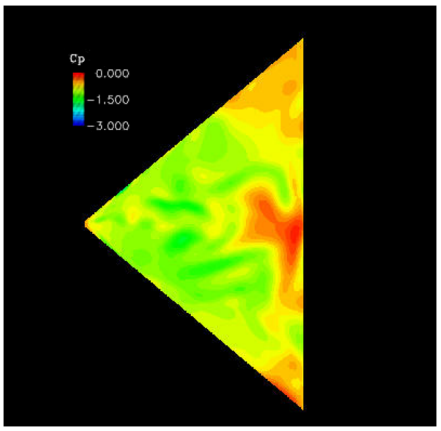

Fig. 21 Surface C_p contours at one instant in time for the coupled aeroelastic problem.

Acknowledgments

This work was produced with U.S. Air Force Office of Scientific Research sponsorship under a task monitored by T. Beutner. This work was supported in part by a grant of high-performance computing (HPC) time from the U.S. Department of Defense HPC Shared Resource Center at the Aeronautical Systems Center (ASC). The first author would also like to acknowledge the National Research Council for providing him with a fellowship to pursue the current research. The authors would like to thank Ismet Gursul and Gordon Taylor of the University of Bath for their valuable discussions about this work and for providing their experimental results.

References

[1] Visbal, M. R., "Computational and Physical Aspects of Vortex Breakdown on Delta Wings," AIAA Paper 95-0585, Jan. 1995.
[2] Rockwell, D., "Three-Dimensional Flow Structures on Delta Wings at High Angle-of-Attack: Experimental Concepts and Issues," AIAA Paper 93-0550, Jan. 1993.
[3] Taylor, G., Schnorbus, T., and Gursul, I., "An Investigation of Vortex Flows over Low Sweep Delta Wings," AIAA Paper 2003-4021, June 2003.
[4] Ol, M., and Gharib, M., "The Passage Toward Stall of Nonslender Delta Wings at Low Reynolds Number," AIAA Paper 2001-2843, June 2001.
[5] Gordnier, R., and Visbal, M., "Higher-Order Compact Difference Scheme Applied to the Simulation of a Low Sweep Delta Wing Flow," AIAA Paper 2003-0620, Jan. 2003.
[6] Gray, J., Gursul, I., and Butler, R., "Aeroelastic Response of a Flexible Delta Wing due to Unsteady Vortex Flows," AIAA Paper 2003-1106, Jan. 2003.
[7] Gordnier, R. E., and Visbal, M. R., "Computation of the Aeroelastic Response of a Flexible Delta Wing at High Angles of Attack," AIAA Paper 2003-1728, Apr. 2003.
[8] Taylor, G., Kroker, A., and Gursul, I., "Passive Flow Control over Flexible Nonslender Delta Wings," AIAA Paper 2005-0865, Jan. 2005.
[9] Gordnier, R. E., and Visbal, M. R., "Numerical Simulation of Nonslender Delta Wing Buffet at High Angle of Attack," AIAA Paper 2004-2047, Apr. 2004.
[10] Vardaki, E., Gursul, I., and Taylor, G., "Physical Mechanisms of Lift Enhancement for Flexible Delta Wings," AIAA Paper 2005-867, Jan. 2005.
[11] Attar, P., and Gordnier, R., "Aeroelastic Prediction of the Limit Cycle Oscillation of a Cropped Delta Wing," AIAA Paper 2005-1915, Apr. 2005.
[12] Pulliam, T., and Steger, J., "Implicit Finite Difference Simulation of Three-Dimensional Compressible Flows," *AIAA Journal*, Vol. 18, No. 2, Feb. 1980, pp. 159–167.
[13] Gordnier, R., "Computation of Limit-Cycle Oscillations of a Delta Wing," *Journal of Aircraft*, Vol. 40, No. 6, 2003, pp. 1206–1208.
[14] Beam, R., and Warming, R., "An Implicit Factored Scheme for the Compressible Navier-Stokes Equations," *AIAA Journal*, Vol. 16, No. 4, Apr. 1978, pp. 393–402.
[15] Gordnier, R., and Visbal, M., "Numerical Simulation of the Unsteady Vortex Structure over a Delta Wing," AIAA Paper 1991-1811, June 1991.
[16] Pulliam, T. and Chaussee, D., "A Diagonal Form of an Implicit Approximate-Factorization Algorithm," *Journal of Computational Physics*, Vol. 39, No. 2, Feb. 1981, pp. 347–363. doi:10.1016/0021-9991(81)90156-X
[17] Morton, S., Melville, R., and Visbal, M., "Accuracy and Coupling Issues of Aeroelastic Navier-Stokes Solutions on Deforming Meshes," AIAA 1997-1085, Apr. 1997.
[18] Gaitonde, D., Edwards, J., and Shang, J., "The Computed Structure of a 3-D Turbulent Interaction Caused by a Cylinder/Offset Flare Juncture,"

AIAA Paper 1995-0230, Jan. 1995.
[19] Jameson, A., Schmidt, W., and Turkel, E., "Numerical Solutions of the Euler Equations by Finite Volume Methods Using Runge-Kutta Time-Stepping Schemes," AIAA Paper 1981-1259, June 1981.
[20] Melville, R., Morton, S., and Rizzetta, D., "Implementation of a Fully Implicit, Aeroelastic Navier-Stokes Solver," AIAA Paper 1997-2039, June 1997.
[21] ANSYS, Software Package, Ver. 7.1, Swanson Analysis Systems, Inc., Canonsburg, PA, 2002.
[22] McMeeking, R., and Rice, J., "Finite Element Formulations for Large Elastic-Plastic Deformation," *International Journal of Solids and Structures*, Vol. 11, May 1975, pp. 601–616. doi:10.1016/0020-7683(75)90033-5
[23] Gordnier, R., and Visbal, M., "Development of a Three-Dimensional Viscous Aeroelastic Solver for Nonlinear Panel Flutter," *Journal of Fluids and Structures*, Vol. 16, No. 4, 2002, pp. 497–527. doi:10.1006/jfls.2000.0434
[24] Farhat, C., and Lesoinne, M., "Two Efficient Staggered Algorithms for the Serial and Parallel Solution of Three-Dimensional Nonlinear Transient Aeroelastic Problems," *Computer Methods in Applied Mechanics and Engineering*, Vol. 182, Nos. 3–4, 2000, pp. 499–515. doi:10.1016/S0045-7825(99)00206-6
[25] Taylor, G., and Gursul, I., "Lift Enhancement over a Flexible Delta Wing," AIAA Paper 2004-2618, June 2004.